Development of an improved spatial reconstruction technique for the HLL method and its applications

Matthew R. Smith [a], K.-M. Lin [b], C.-T. Hung [b], Y.-S. Chen [c], J.-S. Wu [b],*

[a] National Centre for High-Performance Computing, National Applied Research Laboratories, No. 7 R&D Rd. VI, Hsinchu Science Park, Taiwan
[b] Department of Mechanical Engineering, National Chiao Tung University, 1001 Ta-Hsueh Road, Hsinchu 30050, Taiwan
[c] National Space Organization, National Applied Research Laboratories, 8F, 9 Zhan-Ye 1st Road, Hsinchu Science Park, Hsinchu, Taiwan

ARTICLE INFO

ABSTRACT

The integral form of the conventional HLL fluxes are presented by taking integrals around the control volume centred on each cell interface. These integrals are demonstrated to reduce to the conventional HLL flux through simplification by assuming spatially constant conserved properties. The integral flux expressions are then modified by permitting the analytical inclusion of spatially linearly varying conserved quantities. The newly obtained fluxes (which are named HLLG fluxes for clarification, where G stands for gradient inclusion) demonstrate that conventional reconstructions at cell interfaces are invalid and can produce unstable results when applied to conventional HLL schemes. The HLLG method is then applied to the solution of the Euler Equations and Shallow Water Equations for various common benchmark problems and finally applied to a 1D fluid modeling for an argon RF discharge at low pressure. Results show that the correct inclusion of flow gradients is shown to demonstrate superior transient behavior when compared to the existing HLL solver and conventional spatial reconstruction without significantly increasing computational expense.

© 2010 Elsevier Inc. All rights reserved.

1. Introduction

The finite volume method for solution to partial differential equations forms the mainstay of modern computational fluid dynamics (CFD). The development of a conservative scheme for the solution of non-linear systems of hyperbolic conservation laws by Godunov [1] introduced a revelation in the approach to the computation of fluid flow. The resulting family of solvers (known as Godunov type methods) discretizes the flow region into computational regions known as *cells* and use solutions to the Riemann problem at cell interfaces to calculate fluxes of conserved quantities in and out of control volumes.

The original HLL method was developed by Harten et al. [2] as an approximate Riemann solver for use in a Godunov solver. Rather than solving the Riemann problem analytically with knowledge of the behavior of the system (in many cases, an ideal gas), the HLL method solves for the flux in an intermediate region (or *star region*) between cells directly from the governing partial differential equations. A control volume centred on a cell interface is integrated over space and time assuming spatially and temporally constant properties. Through the introduction of the *star region* bounded by two propagating waves, the flux across the interface can be mathematically determined. This allows for the flexible solution of a various number of conservative hyperbolic systems, such as the Shallow Water Equations and the Euler Equations.

The keystone for the HLL method is the assumption of the presence of a single intermediate state bounded to two propagating waves. This is a valid assumption for two variable hyperbolic systems [3] and thus the HLL method is still used for

---

* Corresponding author. Tel.: +886 3 573 1693; fax: +886 3 611 0023.
  E-mail address: chongsin@faculty.nctu.edu.tw (J.-S. Wu).

the solution of the Shallow Water Equations by various authors [3–5]. However, for solutions to other sets of governing equations, such as the Euler Equations, this assumption is invalid [3] due to the presence of two or more intermediate states, each separated by a distinct propagating wave. One solution to this problem was proposed by Toro et al. [6] by the introduction of a contact discontinuity in the HLL expressions. The HLLC (where *C* stands for Contact surface) provides results with less numerical dissipation.

A conventional approach for the extension of the method to higher order spatial accuracy is performed through the inclusion of spatially varying conserved quantities [3,4]. While this does not solve the fundamental problems associated with HLL, it does aid in the removal of numerical dissipation. In such an approach, gradients are used to reconstruct conserved quantities at cell interface locations, following which the ordinary flux expressions are employed for the solution to the Riemann problem.

Presented here is a modification to the HLL method where allowance is made for the inclusion of gradient terms within the flux expressions themselves. First, the original HLL fluxes are presented in integral form and shown to reduce to the original HLL expressions under the assumption of spatially constant properties. The integral form is then re-evaluated when conserved quantities are permitted to vary linearly in space. The resulting fluxes are then combined with the traditional spatial reconstruction concept to produce the HLLG scheme, where the *G* represents the inclusion of gradient terms. This method is then applied to the solution of the Shallow Water Equations, then the Euler Equations and finally the fluid modeling equations for RF discharge at low pressure. The results show an improvement in the numerical diffusion associated with the traditional HLL higher order extensions without significantly increasing computational expense.

2. Numerical method

2.1. Integral form of the original HLL flux expressions

The fluxes developed by Harten et al. [2] are presented here in their complete integral form. Fig. 1 shows a control volume in $x - t$ space covering the region between cells i and $i + 1$ centred on the interface separating the cells at $x = 0$. The region is temporally bound by the limits $t = 0$ and $t = T$. At $t = 0$, waves moving at velocities $S_L(<0)$ and $S_R(>0)$ move away from the discontinuity between the cell interface. If the governing differential equation is given by

$$\frac{\partial U}{\partial t} + \frac{\partial F(U)}{\partial x} = 0, \tag{1}$$

the conditions inside the control volume in the region between $[0,T]$ and $[x_L, x_R]$ can be described by the integral:

$$\int_{x_L}^{0} U_L^0 \, dx + \int_{0}^{x_R} U_R^0 \, dx + \int_{0}^{T} F_L \, dt - \int_{0}^{T} F_R \, dt = \int_{x_L}^{S_L T} U_L^T \, dx + \int_{S_L T}^{S_R T} U_*^T \, dx + \int_{S_R T}^{x_R} U_R^T \, dx, \tag{2}$$

where the subscripts *L* and *R* represent conditions in the left and right cells, respectively, while the superscript *0* and *T* represents conditions at time $t = 0$ and $t = T$, respectively. The subscript $*$ represents conditions in the *star region* between the propagating waves. Rearranging to solve in terms of this star region, we obtain:

$$\int_{S_L T}^{S_R T} U_*^T \, dx = \int_{x_L}^{0} U_L^0 \, dx + \int_{0}^{x_R} U_R^0 \, dx + \int_{0}^{T} F_L \, dt - \int_{0}^{T} F_R \, dt - \int_{x_L}^{S_L T} U_L^T \, dx - \int_{S_R T}^{x_R} U_R^T \, dx. \tag{3}$$

This equation assumes nothing regarding variation of fluxes *F* or conserved quantities *U* within space and time. The only assumptions made are in the presence of the two propagating waves surrounding a single intermediate region at $x = 0$. Fig. 2
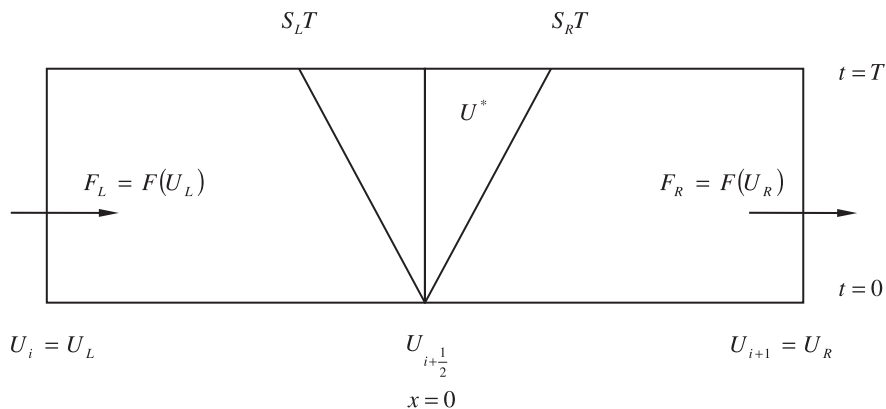

Fig. 1. Control volume bounded by the centre of cell i and cell $i + 1$, with the interface between each located at $x = 0$.

shows the revised $x - t$ diagram focusing on the left cell only. Using the same method of integrating conserved quantities over space and fluxed quantities over time obtains:

$$\int_{x_L}^{0} U_L^0 \, dx + \int_0^T F_L \, dt - \int_0^T F_* = \int_{x_L}^{S_L T} U_L^T \, dx + \int_{S_L T}^{0} U_*^T \, dx. \tag{4}$$

We further assume that the average state over the region between $x = S_L T$ and $x = S_R T$ is the same as the average between the region $x = S_L T$ and $x = 0$, or:

$$\frac{1}{-S_L T} \int_{S_L T}^{0} U_*^T \, dx = \frac{1}{S_R T - S_L T} \int_{S_L T}^{S_R T} U_*^T \, dx, \tag{5}$$

or:

$$\int_{S_L T}^{0} U_*^T \, dx = \frac{-S_L}{S_R - S_L} \int_{S_L T}^{S_R T} U_*^T \, dx. \tag{6}$$

This assumption provides us the knowledge required to solve for our desired quantity, the flux F^*. Combining Eqs. 3,4,6 provide the complete integral form of the total flux F^* over time step T:

$$\int_0^T F_* = \int_{x_L}^{0} U_L^0 \, dx - \int_{x_L}^{S_L T} U_L^T \, dx + \int_0^T F_L \, dt - \int_{S_L T}^{0} U_*^T \, dx$$

$$= \int_{x_L}^{0} U_L^0 \, dx - \int_{x_L}^{S_L T} U_L^T \, dx + \int_0^T F_L \, dt$$

$$+ \frac{S_L}{S_R - S_L} \left(\int_{x_L}^{0} U_L^0 \, dx - \int_{x_L}^{S_L T} U_L^T \, dx + \int_0^{x_R} U_R^0 \, dx - \int_{S_R T}^{x_R} U_R^T \, dx + \int_0^T F_L \, dt - \int_0^T F_R \, dt \right). \tag{7}$$

2.2. Simplification of the integral form

The integral form of the HLL fluxes can be evaluated by making assumptions about the integral expressions. Assuming the regions to the left of the left moving wave and to the right of the right moving wave remain untouched over the period of a time step T, the following simplifications can be made:

$$\int_{x_L}^{0} U_L^0 \, dx - \int_{x_L}^{S_L T} U_L^T \, dx \approx \int_{S_L T}^{0} U_L \, dx,$$

$$\int_0^{x_R} U_R^0 \, dx - \int_{S_R T}^{x_R} U_R^T \, dx \approx \int_0^{S_R T} U_R \, dx. \tag{8}$$

Note these assumptions still permit spatially varying quantities of U and only assume that regions outside propagating waves S_L and S_R. From a (more mathematical) perspective, this step represents a simple resizing of the control volume employed for the flux computation. Using these assumptions, the modified equation simplifies to:

$$\int_0^T F_* = \int_{S_L T}^{0} U_L \, dx + \int_0^T F_L \, dt + \frac{S_L}{S_R - S_L} \left(\int_{S_L T}^{0} U_L \, dx + \int_0^{S_R T} U_R \, dx + \int_0^T F_L \, dt - \int_0^T F_R \, dt \right). \tag{9}$$
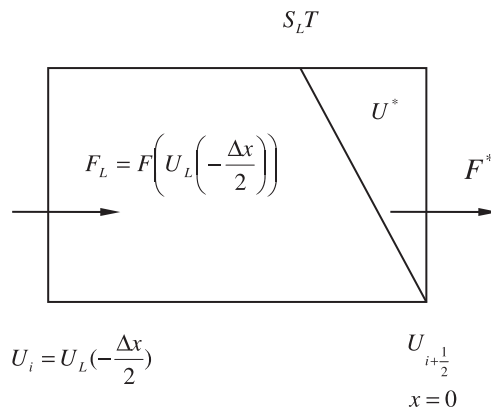

Fig. 2. Control volume centred bounded by the centre of cell U_i, the interface between cell i and cell $i + 1$ at $x = 0$, time $t = 0$ and $t = T$.
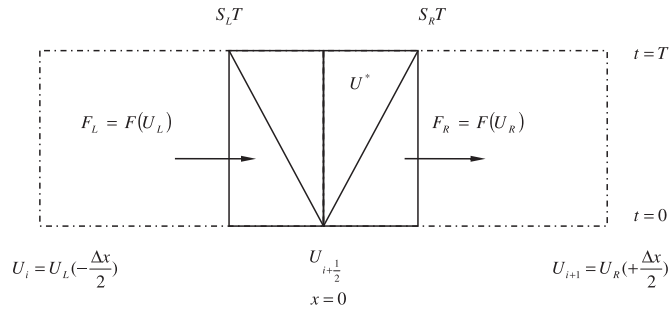
Fig. 3. Revised control volume between propagating waves moving with speeds S_L and S_R. The fluxes through the left and right surfaces of the control volume are calculated using values of U at locations S_{RT} and S_{LT} thus allowing the assumption of constant F_L and F_R over time T.

Notice now that the equation for the total flux across the interface is now only governed by integrals bounded by the left and right moving waves. This control volume is shown together with the remaining cell topography in Fig. 3. By assuming that the quantities U remain spatially constant (i.e. monotonic in nature) and the fluxes are temporally constant we find (for example):

$$\int_{S_L T}^{0} U_L \, dx = -S_L T U_L,$$
$$\int_{0}^{T} F_L \, dt = F_L T. \tag{10}$$

The consequence of the latter assumption is that the flux F_L is not permitted to change over time (or alternatively, F_L represents the average value of F at that location) and must be calculated accordingly. After applying the said simplifications and evaluating the complete integral expression in Eq. (7), the original HLL flux expressions [2] are obtained.

2.3. Inclusion of spatial variation of conserved quantities

The assumption of constant conserved quantities U made in Eq. (10) results in spatially first order accuracy. We can instead allow U to vary linearly in space such that:

$$U_L(x) = U_L^{i+\frac{1}{2}} + \left(\frac{dU}{dx}\right)_L x, \tag{11}$$

where superscript $i + 1/2$ indicates conditions at the cell interface where $x = 0$ and subscript L refers to conditions on the left side of the interface. This is demonstrated in Fig. 4. The gradient term is calculated using finite differences together with a selected slope limiter to maintain positivity. A commonly used example is the MINMOD limiter [7]:

$$\left(\frac{dU}{dx}\right)_{eff} = \text{MINMOD}\left[\left(\frac{dU}{dx}\right)_F, \left(\frac{dU}{dx}\right)_B\right], \tag{12}$$
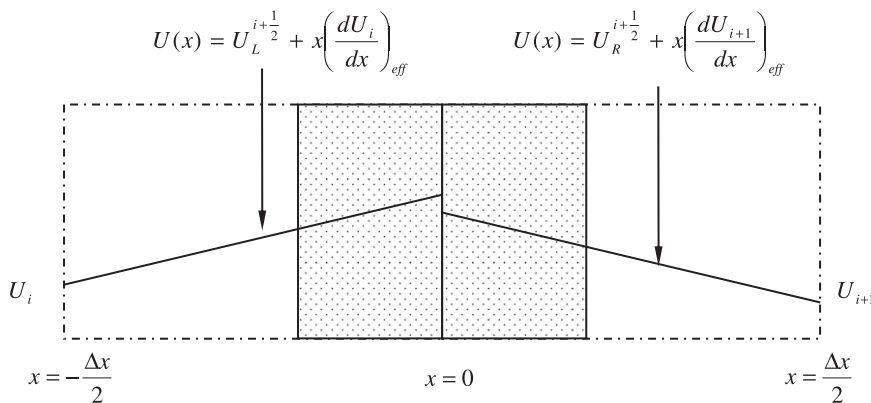

Fig. 4. Spatial reconstruction of conserved quantity U. The coordinate system must be consistent with that used in the HLL flux derivation. The revised control volume (shown) is bounded by $S_L \Delta t < x < S_R \Delta t$.

where "*eff*" indicates an effective gradient, subscripts F and B are the forward and backward differences, respectively. The MINMOD (or Minimum Modulus) function is given by:

$$\text{MINMOD}[a, b] = \begin{cases} 0, & \text{IF SIGN}(ab) < 0, \\ a, & \text{IF (SIGN}(ab) > 0) \text{ AND } (|a| < |b|), \\ b, & \text{IF (SIGN}(ab) > 0) \text{ AND } (|b| < |a|). \end{cases} \tag{13}$$

A general improvement to the MINMOD limiter is the Monotonized Central Difference (MC) limiter [8]. This has been used in the previous applications of HLL applied to solutions of the Euler and Shallow Water equations [3,4] in addition to the kinetic theory based Euler solver QDS (Quiet Direct Simulation) [9]. The MC limiter is defined as:

$$\left(\frac{dU}{dx}\right)_{eff} = \text{MINMOD}\left[\left(\frac{dU}{dx}\right)_C, \alpha \cdot \text{MINMOD}\left[\left(\frac{dU}{dx}\right)_F, \left(\frac{dU}{dx}\right)_B\right]\right]. \tag{14}$$

The variable alpha is used to control dissipation in the scheme and is set to $\alpha = 1$ or 2 to limit dissipation to a minimum (setting $\alpha = 0$ recreates a spatially first order scheme). Assuming a uniform cell width Δx, the interface values can be found using the gradient information such that:

$$U_L^{i+\frac{1}{2}} = U_L + \left(\frac{dU}{dx}\right)_L \frac{\Delta x}{2} \rightarrow U_R^{i+\frac{1}{2}} = U_R - \left(\frac{dU}{dx}\right)_R \frac{\Delta x}{2}. \tag{15}$$

Substituting these obtains the simple expressions:

$$\begin{aligned} U_L(x) &= U_L + \left(\frac{dU}{dx}\right)_L \left(x + \frac{\Delta x}{2}\right), \\ U_R(x) &= U_R + \left(\frac{dU}{dx}\right)_R \left(x - \frac{\Delta x}{2}\right). \end{aligned} \tag{16}$$

This allows an alternate evaluation of the integral form of the HLL flux expressions. Substituting and evaluating the integral obtains the final flux:

$$\begin{aligned} \overline{F_*} \approx &\left(\frac{1}{S_R - S_L}\right)\left\{F\left(U_L + \left(\frac{dU}{dx}\right)_L\left(\frac{\Delta x}{2} + S_L T\right)\right)S_R - F\left(U_R - \left(\frac{dU}{dx}\right)_R\left(\frac{\Delta x}{2} - S_R T\right)\right)S_L \right. \\ &\left. - S_R S_L\left(\left(U_R - \left(\frac{dU}{dx}\right)_R\left(\frac{\Delta x}{2} - \frac{S_R T}{2}\right)\right) - \left(U_L + \left(\frac{dU}{dx}\right)_L\left(\frac{\Delta x}{2} + \frac{S_L T}{2}\right)\right)\right)\right\}. \end{aligned} \tag{17}$$

The average flux represented in Eq. (17) can be rewritten in terms of the original HLL flux expression:

$$\overline{F_*} \approx \frac{F\left(U_L^1\right)S_R - F\left(U_R^1\right)S_L - S_R S_L\left(U_R^2 - U_L^2\right)}{S_R - S_L}, \tag{18}$$

where superscripts 1 and 2 indicate reconstruction at locations at distances ST and $ST/2$ away from the cell interface respectively. Care must be taken with the reconstruction when $S_L > 0$ or $S_R < 0$ to avoid over-reconstruction in regions each respective cell when upwind fluxes are used.

2.4. Comparison against conventional higher order extension

The original HLL scheme assumes monotonic conditions across each cell and is thus first order accurate in space. In the decades which have followed since HLL's developments, a large family of methods for extension of spatial accuracy have been developed. Many of these methods use cell-averaged states to compute gradients for use in reconstruction at cell interfaces [10–16]. For example, recent developments such as General Riemann Problem (GRP) schemes [14–16] employ spatial reconstruction to determine conditions at the interface:

$$U_{j+1/2,+}^n = U_j^n + \left(\frac{dU}{dx}\right)_j^n \frac{\Delta x}{2}, \quad U_{j+1/2,-}^n = U_{j+1}^n - \left(\frac{dU}{dx}\right)_{j+1}^n \frac{\Delta x}{2}, \tag{19}$$

where superscript n indicates conditions at step n and $+/-$ represents the left/right side of the interface at $j + 1/2$, respectively. Following this reconstruction, GRP schemes differ only from conventional second order methods through employing analytical expressions for $\left(\frac{dU}{dt}\right)_{j+1/2}^n$ to advance the solution [15]:

$$U_{j+1/2}^{n+1/2} = U_{j+1/2}^n + \left(\frac{dU}{dt}\right)_{j+1/2}^n \frac{\Delta t}{2}, \tag{20}$$

where $U_{j+1/2}^n = R^A\left(U_{j+1/2,+}^n, U_{j+1/2,-}^n\right)$ is the solution to the Riemann problem at step n. These conditions are then used to compute the fluxes across the interface. The inclusion of this step provides the extension to higher order temporal accuracy without relying on more approximate temporal extensions as often employed in conventional MUSCL schemes [17]. In the

absence of this additional step, such schemes are identical to (temporally first order accurate) MUSCL type extensions [15]. The integral (balance) approach demonstrated here is not applicable to the additional step employed by GRP type schemes since investigations presented here are limited to first order temporal accuracy (refer to integrals given in Eq. (10)). Following conventional reconstruction at cell interfaces and application of the original HLL fluxes upon reconstructed states, the flux is:

$$\overline{F}_* \approx \frac{F\left(U_L + \left(\frac{dU}{dx}\right)_L\left(\frac{\Delta x}{2}\right)\right)S_R - F\left(U_R - \left(\frac{dU}{dx}\right)_R\left(\frac{\Delta x}{2}\right)\right)S_L - S_R S_L\left(\left(U_R - \left(\frac{dU}{dx}\right)_R\left(\frac{\Delta x}{2}\right)\right) - \left(U_L + \left(\frac{dU}{dx}\right)_L\left(\frac{\Delta x}{2}\right)\right)\right)}{S_R - S_L}. \tag{21}$$

Although a trivial exercise in mathematics, comparison against Eqs. (17) and (21) reveals that conventional spatial reconstruction (as employed by MUSCL and/or GRP schemes) is inconsistent when HLL is used for flux computation. The formal inclusion of gradients in the HLL flux derivation reveals that two reconstructions are required, at distances ST and $0.5ST$ on each side from the cell interface respectively, for the flux function evaluation and the U term typically associated with the anti-diffusion component. This might seem trivial given the demonstrated performance of these schemes [3,4]. Indeed, when using most popular limiting functions (e.g. MINMOD) the flaws associated with this oversight are very difficult to perceive for some problems. However, demonstration of flaws resulting from this oversight is possible.

2.5. Implementation of HLLG fluxes

The calculation of the modified HLL (or HLLG) fluxes in one dimension is shown by the following steps and supplemented by the diagram shown in Fig. 5:

1. Estimate the wave speeds S_L and S_R using the cell-centred values. The value of these wave speeds differ depending on the system of equations solved. Review into the computation of wave speed estimates lies outside the scope of this investigation – details can be found in [3–5].

2. Reconstruct U at the locations within the control volume shown in Fig. 5:

$$\begin{aligned}
f_L^1 &= \min\left(\frac{\Delta x}{2} + S_L T, \frac{\Delta x}{2}\right), \quad f_R^1 = \max\left(-\frac{\Delta x}{2} + S_R T, -\frac{\Delta x}{2}\right), \\
f_L^2 &= \min\left(\frac{\Delta x}{2} + \frac{S_L T}{2}, \frac{\Delta x}{2}\right), \quad f_R^2 = \max\left(-\frac{\Delta x}{2} + \frac{S_R T}{2}, -\frac{\Delta x}{2}\right), \\
U_L^1 &= U_L + f_L^1\left(\frac{dU_L}{dx}\right)_{eff}, \quad U_R^1 = U_R - f_R^1\left(\frac{dU_R}{dx}\right)_{eff}, \\
U_L^2 &= U_L + f_L^2\left(\frac{dU_L}{dx}\right)_{eff}, \quad U_R^2 = U_R - f_R^2\left(\frac{dU_R}{dx}\right)_{eff}.
\end{aligned} \tag{22}$$

3. Calculate the flux across the interface. If either $S_L > 0$ or $SR < 0$, the respective upwind fluxes are used $\left(S_L > 0 : F_* = F\left(U_L^1\right), S_R < 0 : F_* = F\left(U_R^1\right)\right)$. Otherwise, the revised HLL (or HLLG) flux is used:
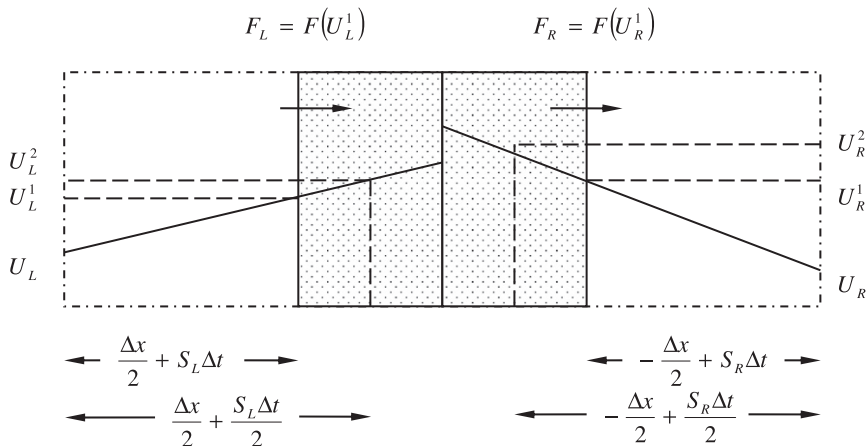

Fig. 5. Reconstruction locations for the revised (HLLG) expressions showing the control volume employed during the analysis. Fluxes F are computed using values of U reconstructed at the edge of the control volume while the value of conserved quantities U employed in the HLLG flux expression are reconstructed in the centre of each half of the control volume.

$$\overline{F_*} \approx \frac{F\left(U_L^1\right)S_R - S_R - F\left(U_R^1\right)S_L - S_R S_L\left(U_R^2 - U_L^2\right)}{S_R - S_L}. \tag{23}$$

3. Results and discussion

3.1. 2D shallow water equations – dam break

An ideal two dimensional circular dam break problem is considered. The two dimensional dam break simulation is performed to test the shock capturing properties of HLLG. The governing equations employed are the Shallow Water Equations, defined as:

$$\frac{\partial U}{\partial t} + \frac{\partial F}{\partial x} + \frac{\partial G}{\partial y} = 0,$$
$$\frac{\partial}{\partial t}\begin{bmatrix} \phi \\ \phi u \\ \phi v \end{bmatrix} + \frac{\partial}{\partial x}\begin{bmatrix} \phi u \\ \phi u^2 + \frac{\phi^2}{2} \\ \phi u v \end{bmatrix} + \frac{\partial}{\partial y}\begin{bmatrix} \phi v \\ \phi u v \\ \phi v^2 + \frac{\phi^2}{2} \end{bmatrix} = 0, \tag{24}$$

where $\phi = gh$, g is gravitation acceleration (≈ 9.81) and h is the water level. The values u and v are the velocity in the x and y directions, respectively. A simple method for estimating the wave speeds is $S_L = \text{MIN}[V_L - a_L, V_R - a_R]$ and $S_R = \text{MAX}[V_L + a_L, V_R + a_R]$ [3–5] where $a_L = \sqrt{\phi_L}$ and $a_R = \sqrt{\phi_R}$ are the characteristic speeds of propagation and V_L, V_R are the velocities of flow normal to the interface. A circular region of water of elevation h_{IN} is elevated and separated from the surrounding water of elevation h_{OUT} by an infinitely thin separating dam. The initial water levels are:

$$h_0(x) = \begin{cases} h_{IN} = 2.5 \text{ m}, & (x - x_c)^2 + (y - y_c)^2 \leqslant R, \\ h_{OUT} = 0.5 \text{ m}, & (x - x_c)^2 + (y - y_c)^2 > R, \end{cases} \tag{25}$$

where R is the radius of the circular region $R = 2.5$ m and subscript c indicates the location of the centre of the elevated region (x_c, y_c). The water is assumed to be at rest ($u = v = 0$). The computational domain extends over $L = H = 40$ m and results are presented for a regular Cartesian computational grid of 200 by 200 cells after a flow time of 5 s. The time step is adaptive to ensure a constant maximum CFL of 0.5. The results are expected to be radially symmetric in nature due to the radially symmetric nature of the initial conditions.

Various figures of the resulting water level after 5 s are shown in Fig. 6. The oscillations shown in the HLL results strongly affect the flow field. The oscillations are weaker along the horizontal ($\theta = 0°$) and vertical ($\theta = 90°$) lines. This may mislead one to interpret the errors as due to poor mesh alignment. Indeed, employing a circular grid will remove most of these oscillations. However, these errors are not characteristic of errors resulting from direction decoupling [18] and are not consistent with the HLLG results, as also demonstrated by the water levels shown in Fig. 6. There are major differences between the diagonal and horizontal results shown in the HLLG solutions, thus ruling out direction coupling and poor grid alignment as the cause of the oscillations present in the HLL results. The spatial reconstruction of conserved properties is performed using finite differences with the MINMOD limiter [7], which is known to be diffusive. Thus, the same simulations are repeated using the Monotonized Central Difference (MC) limiter [8] with $\alpha = 2$. The influence of the instabilities presented in the HLL solution is dominant, as demonstrated in Fig. 7. However, the influence of the new limiting function has only minimal influence on the HLLG results, which still remain radially symmetric with only minor oscillations in regions where flows are unaligned with the computational grid. The above shows that the use of HLLG scheme greatly improves the water shallow equation simulation and reduces sensitivity to the selected limiter when compared to the use of conventional HLL reconstruction.

3.2. 1D Euler equations – shock/acoustic wave interaction

The one dimensional Euler Equations are applied to Shu and Osher's simulation of a shock/acoustic wave interaction [19,20]. The one dimensional Euler Equations, without source terms in conservation form, are:

$$\frac{\partial U}{\partial t} + \frac{\partial F}{\partial x} = 0,$$
$$\frac{\partial}{\partial t}\begin{bmatrix} \rho \\ \rho u \\ E \end{bmatrix} + \frac{\partial}{\partial x}\begin{bmatrix} \rho u \\ \rho u^2 + p \\ u(E + p) \end{bmatrix} = 0, \tag{26}$$

where ρ is the gas density, u is the velocity, p is the pressure computed from the ideal gas law ($p = \rho RT$) and the energy E is given by $E = \rho(1/2u^2 + C_V T)$ where C_v is the specific heat constant at constant volume and T is the temperature. The initial conditions for the problem are $[\rho, u, p] = [3.857143, 2.629369, 10.33333]$ in the region $-5 \leqslant x < -4$ and $[\rho, u, p] = [1 + 0.2\sin(5x), 0, 1]$ for
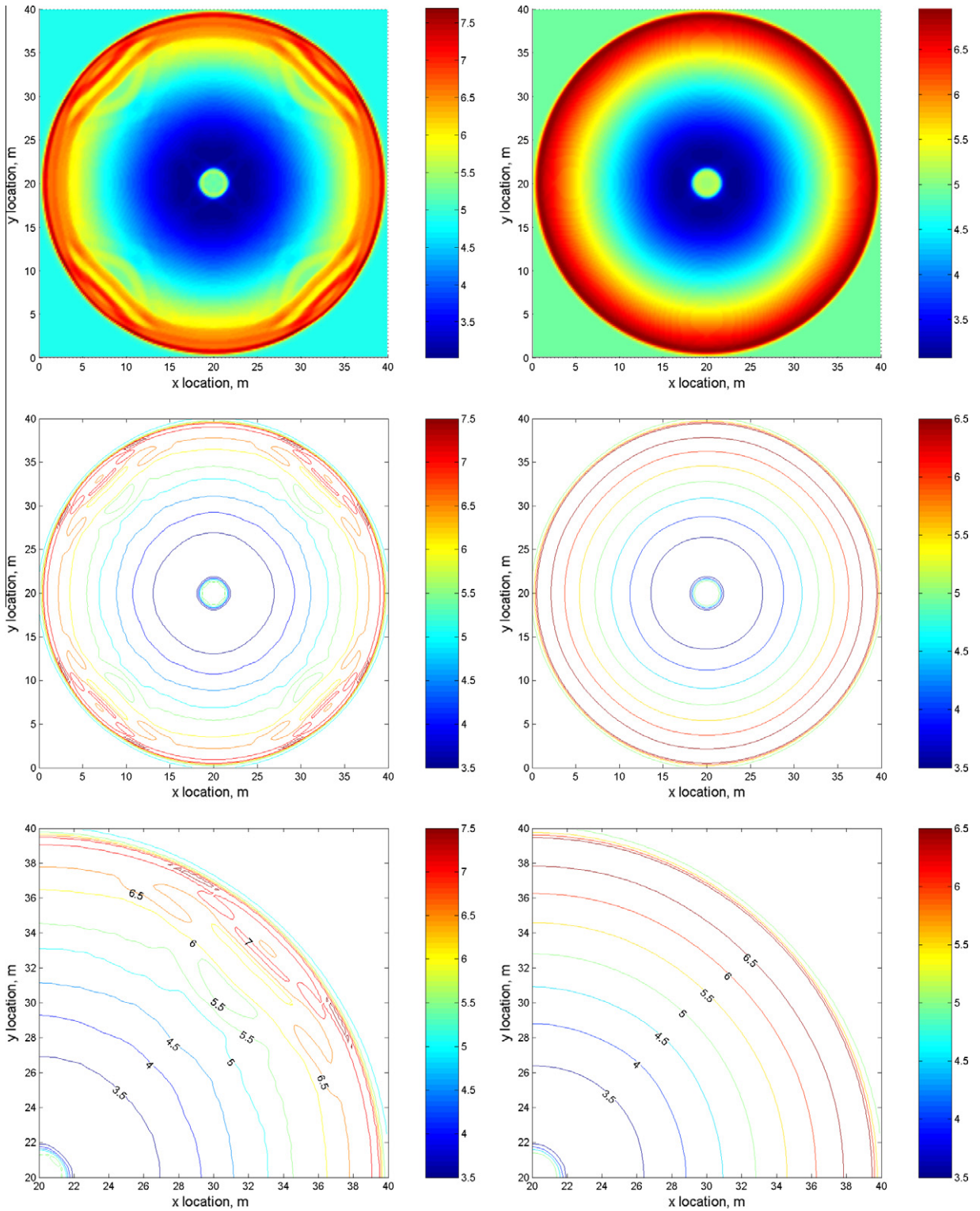
Fig. 6. Values of geopotential (U) taken from solutions to the 2D dam break problem as computed by HLL (left) and HLLG (right). Each simulation employed 200×200 cells and a constant maximum CFL of 0.5. Gradients employed for reconstruction are calculated by finite differences and limited by the MINMOD limiter. Contours are displayed at levels of 0.5.

$-4 \leqslant x < 5$. The gas is inviscid and ideal ($\gamma = 1.4$) and the flow is allowed to develop until flow time $t = 1.8$. Wave speed computation is similar to that employed above except that the characteristic propagation speed is now the local speed of sound
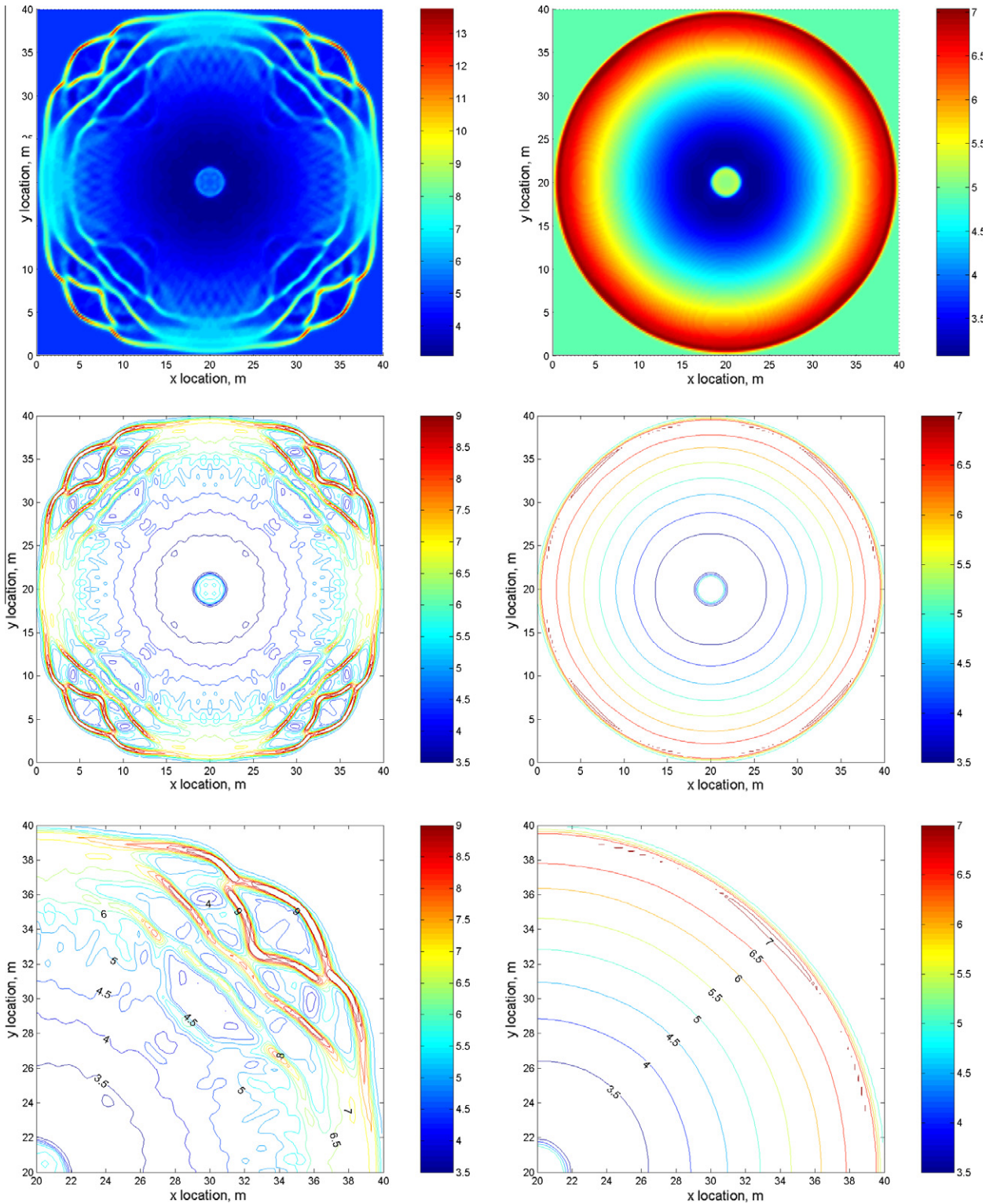
Fig. 7. Values of geopotential (Φ) taken from solutions to the 2D dam break problem as computed by HLL (left) and HLLG (right). Each simulation employed 200×200 cells and a constant maximum CFL of 0.5. Gradients employed for reconstruction are calculated by finite differences and limited by the MC limiter. Contours are displayed at levels of 0.5.

$a = (\gamma R T)^{1/2}$. Resulting density contours from both the proposed HLLG solver and HLL solver are presented in Fig. 8. Each simulation uses 400 cells with a constant maximum CFL of 0.1 enforced. The MC limiter ($\alpha = 2$) is employed by both solutions to
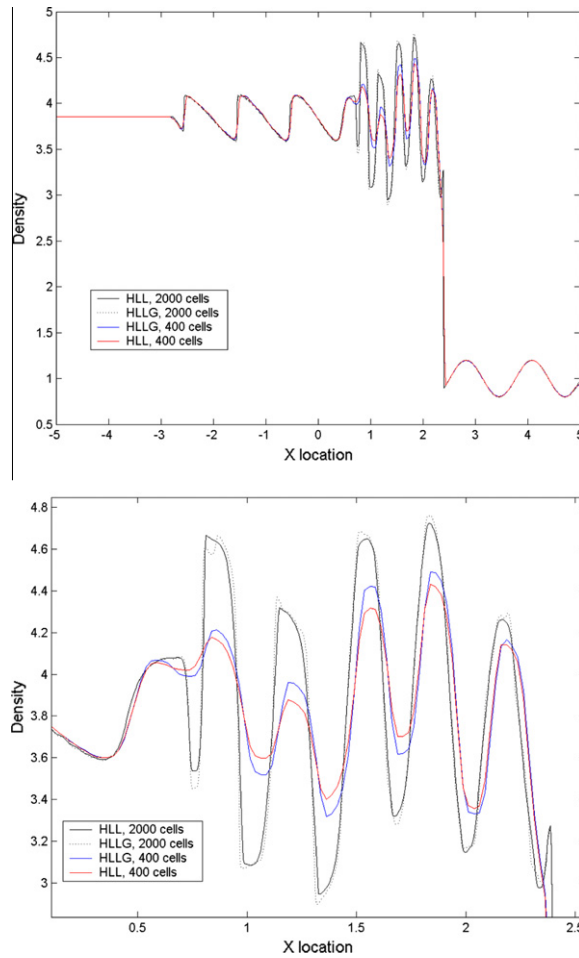
Fig. 8. One dimensional shock/acoustic wave interaction problem. Results show profiles of density for the conventionally extended HLL solver and the proposed HLLG extension. All simulations employ 400 cells with an enforced maximum CFL = 0.1. HLL and HLLG simulations using 2000 cells are employed as benchmark results.

limit the spatial reconstruction to first order in spurious regions. It can be seen that the result obtained by HLLG provides a closer comparison to the benchmark solution shown than the conventionally reconstructed second order HLL results.

3.3. 2D Euler equations – blast wave

The two dimensional Euler Equations are applied to the simulation of a temperature driven radially symmetric blast wave [18]. The two dimensional Euler Equations are:

$$
\frac{\partial U}{\partial t} + \frac{\partial F}{\partial x} + \frac{\partial G}{\partial y} = 0,
$$

$$
\frac{\partial}{\partial t} \begin{bmatrix} \rho \\ \rho u \\ \rho v \\ E \end{bmatrix} + \frac{\partial}{\partial x} \begin{bmatrix} \rho u \\ \rho u^2 + p \\ \rho u v \\ u(E+p) \end{bmatrix} + \frac{\partial}{\partial y} \begin{bmatrix} \rho v \\ \rho v u \\ \rho v^2 + p \\ v(E+p) \end{bmatrix} = 0,
\tag{27}
$$

where ρ is the gas density, u and v are velocities in the x and y directions, respectively, and p is the pressure computed from the ideal gas law ($p = \rho R T$). The internal energy E is given by $E = \rho(1/2(u^2 + v^2) + C_V T)$. A region of high temperature gas of radius $r = 0.1L$ is separated by an imaginary diaphragm and surrounded by a region of low temperature gas $\left(T_H T_L^{-1} = 100\right)$. At $t = 0$, the diaphragm is removed and the resulting blast wave propagates outwards in a radially symmetric fashion. The resulting contours of density and velocity are shown in Fig. 9. Both solvers are shown to possess characteristic direction decoupling errors with higher regions of density along the diagonal [18]. The conventional extension of HLL to sec-
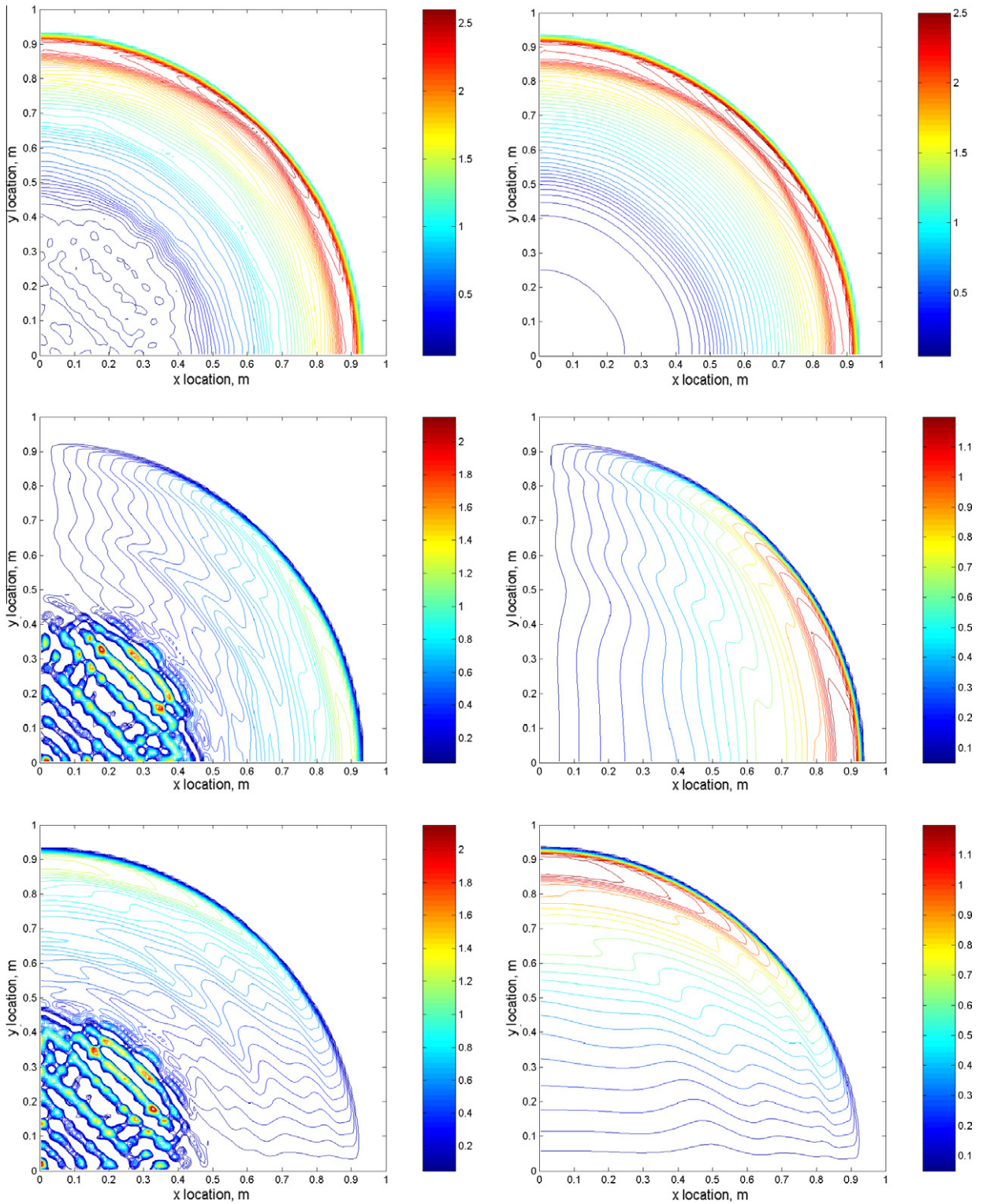
Fig. 9. Two dimensional temperature driven blast wave problem contours of density [top], *x* velocity [center] and *y* velocity [bottom] from proposed HLLG reconstruction [right] and conventional HLL reconstruction [left]. Gradients employed for reconstruction are calculated by finite differences and limited by the MC limiter ($\alpha = 0$). Both simulations employ 100×100 cells with an enforced maximum CFL number of 0.5. Results are shown after flow time $t = 0.25$.

ond order spatial accuracy using the MC limiter results in a large number of asymmetric, spurious oscillations which are not present in the HLLG results.

3.4. 2D Euler equations – supersonic flow over a forward facing step

The proposed HLLG method is applied to the simulation of supersonic flow over a forward facing step [21]. The problem geometry and boundary conditions are shown in Fig. 10. An ideal gas (γ = 1.4) with an initial Mach number of M = 3 every-where. This problem is commonly used to verify gas flow solvers. The density contours computed by both methods are presented in Fig. 11 after the flow has been advanced to flow time t = 4.0. In this instance, the differences between the HLLG and the conventionally extended HLL solution are negligible.
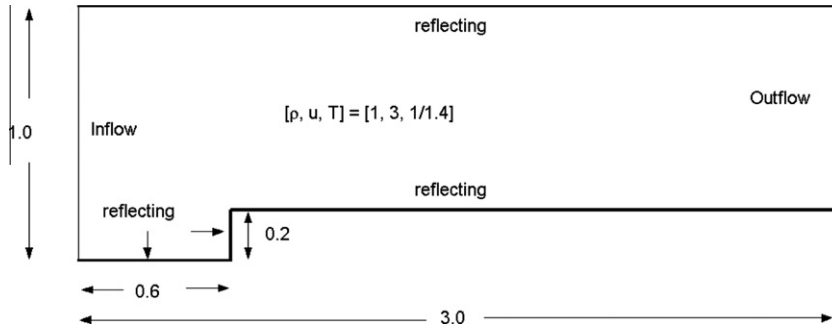

Fig. 10. Supersonic flow over a forward facing step problem. All surfaces are reflective with exception of the supersonic outflow located at x = 3, $0.2 \leqslant y \leqslant 1.0$ and the inflow located at x = 0.0.
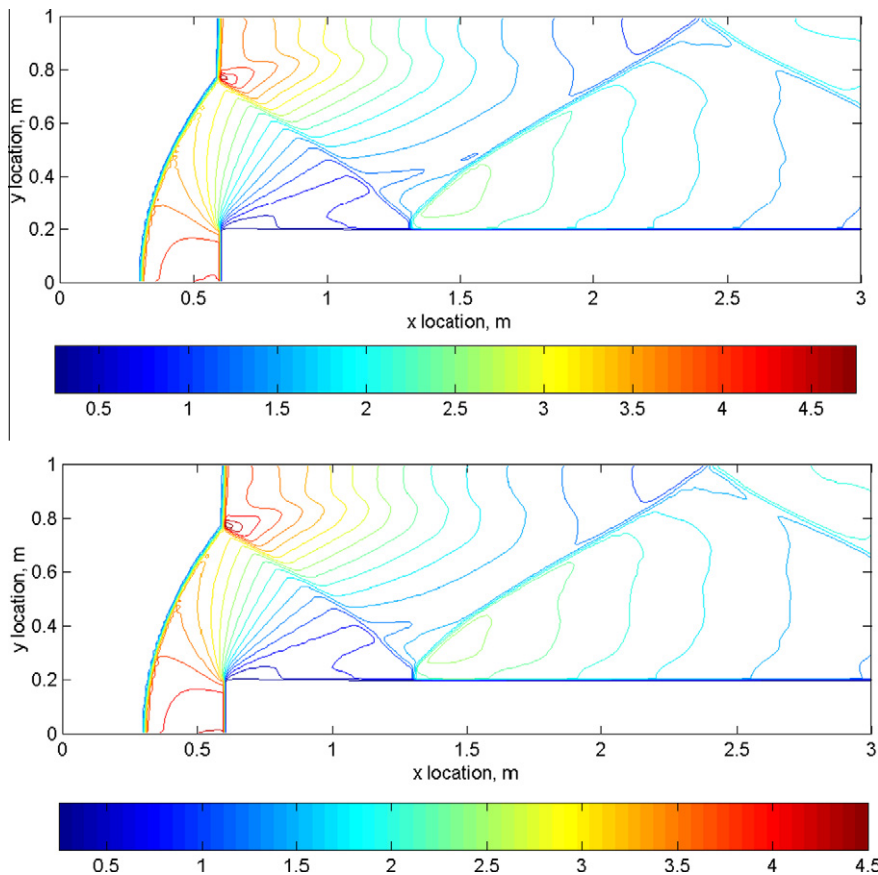

Fig. 11. Supersonic flow over a forward facing step problem after t = 4 showing contours of density computed by conventionally extended second order HLL [top] and the proposed HLLG second order extension [bottom]. Contours of density are shown every 0.25. The simulation employs 300×100 cells with CFL = 0.25.

3.5. 2D Euler equations – shock bubble interaction

We apply the proposed reconstruction method to the simulation of a shock wave moving over a low density bubble [19]. The shock-bubble problem solved is shown in Fig. 12. The gas is assumed ideal ($\gamma = 1.4$). Symmetry can be exploited along $y = 0$ and only half the problem need be considered. The flow is advanced until flow time $t = 0.2$. All simulations employed 200×200 cells with varying CFL numbers (0.5–0.75). Presented in Fig. 13 are numerical Schlierens (indicative of gradients of density) demonstrating similar oscillatory instabilities in regions where flows are misaligned with the computational grid. While the HLLG results demonstrate these errors (which are dependent on the CFL number employed), the numerical "wriggles" present in the HLL solution are much more severe. Thus, for any given CFL number, the result provided by the HLLG reconstruction will prove less-prone to numerical instability than the original extension of HLL to higher order accuracy.

3.6. 1D argon RF plasma simulation

Finally, the simulation of parallel-plate argon RF ($f = 13.56$ MHz) coupled capacitively discharge (CPC) is investigated using the HLLG solver. The motion of charged and neutral species is governed by a series of general transport equations:

$$
\begin{aligned}
\frac{\partial n_e}{\partial t} + \frac{\partial \Gamma_e}{\partial x} &= S_e, \\
\frac{\partial n_i}{\partial t} + \frac{\partial \Gamma_i}{\partial x} &= S_i, \\
\frac{\partial n_n}{\partial t} + \frac{\partial \Gamma_n}{\partial x} &= S_n, \\
\frac{\partial (n_e \langle \varepsilon \rangle)}{\partial t} + \frac{\partial \Gamma_E}{\partial x} &= -e \cdot \Gamma_E \cdot E + S_E,
\end{aligned}
\tag{28}
$$

where subscripts e, i and n represent the electron, ion and neutral species number density, respectively. By applying drift-diffusion approximation [15], the flux expressions (Γ) for each equation are:

$$
\begin{aligned}
\Gamma_e &= -\mu_e E n_e - D_e \frac{\partial n_e}{\partial x}, \\
\Gamma_i &= \mu_i E n_i - D_i \frac{\partial n_i}{\partial x}, \\
\Gamma_\varepsilon &= -\frac{5}{3} \mu_e E n_e \langle \varepsilon \rangle - \frac{5}{3} D_i \frac{\partial (n_e \langle \varepsilon \rangle)}{\partial x},
\end{aligned}
\tag{29}
$$

where the coefficients of mobility (μ) and diffusion coefficients (D) control the general motion of each species. The electron mobility and diffusion coefficients are functions of the electron temperature, computed from the electron energy density $\langle \varepsilon \rangle = \frac{3}{2} k_B T_e$, with values taken from BOLSIG [22]. Charged species are influenced by the presence of an electric field $E = -\nabla \Phi$, where the potential field as predicted by the Poisson Equation:

$$
\frac{\partial}{\partial x} \left(\varepsilon \frac{\partial \Phi}{\partial x} \right) = -e \left(\sum n_i - \sum n_e \right).
\tag{30}
$$

The potential field is solved implicitly using a conventional finite difference discretization and either a conjugate gradient or GMRES solver. A semi-implicit formulation [23] is required for computation of the source terms in Eq. (30) – otherwise the
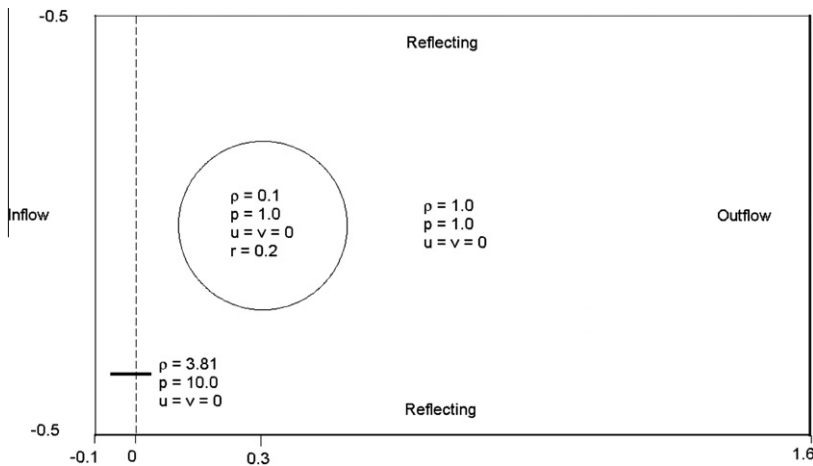

Fig. 12. Shock-Bubble interaction problem with a shock wave located at $x = 0$ propagating into a low-density bubble of equal pressure. All simulations exploit symmetry around $y = 0$.
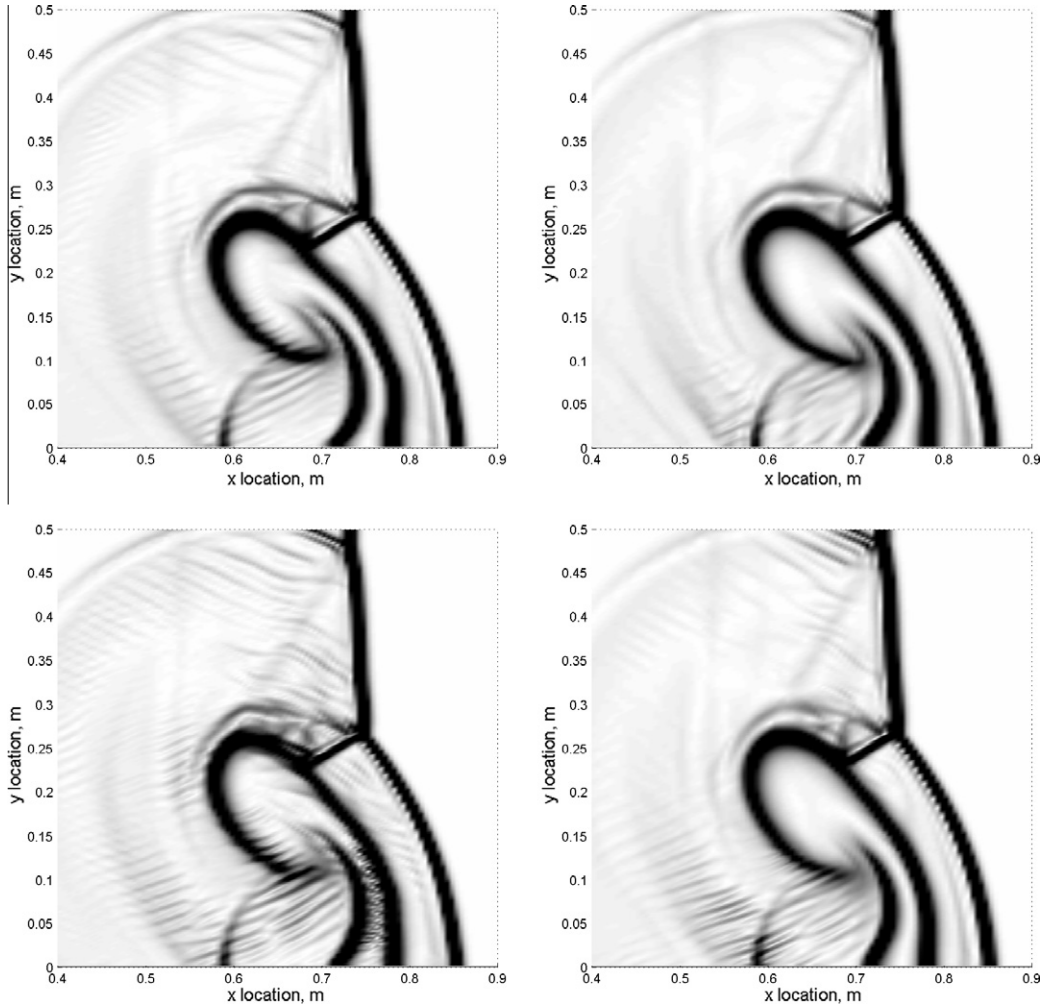
Fig. 13. Numerical Schlierens taken from simulation results of HLL (left) and HLLG (right). Both simulations show results after $t = 0.2$ with CFL numbers of 0.5 (top) and 0.75 (bottom) using 200×200 cells. Gradients employed for reconstruction are calculated by finite differences and limited by the MINMOD limiter.

solution (regardless of approach) quickly becomes unstable. The diffusivity of ions is given by the Einstein relation with coefficients of mobility computed from [24]:

$$\mu_i = \frac{0.574T}{P\sqrt{m\alpha}}, \tag{31}$$

where T and P are the background gas temperature and pressure, respectively, m is the reduced mass (given in AMU) and α is the polarizability of the background gas (more details can be found in [24]). Neutral species use diffusion coefficients computed from the Chapman–Enskog theory of gases [25]. The source terms present in the governing fluid modeling equations (Eq. (28)) (for example, S_e) describe the production of species resulting from plasma and chemical reactions. These reactions considered here are [26–29]:

$$
\begin{aligned}
&e^- + Ar \rightarrow e^- + Ar, \\
&e^- + Ar \rightarrow 2e^- + Ar^+, \\
&e^- + Ar \rightarrow e^- + Ar_m, \\
&e^- + Ar \rightarrow e^- + Ar_r, \\
&e^- + Ar_m \rightarrow 2e^- + Ar^+, \\
&e^- + Ar_m \rightarrow e^- + Ar_r, \\
&2Ar_m \rightarrow Ar + Ar^+ + e^-, \\
&Ar_r \rightarrow Ar, \\
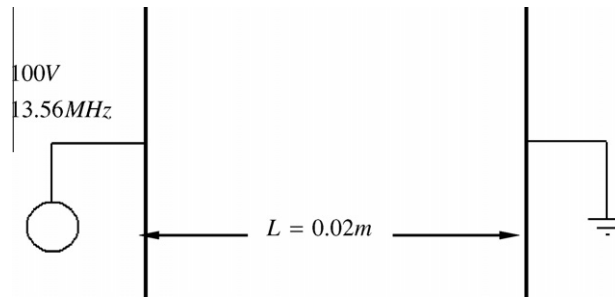&Ar + Ar_m \rightarrow 2Ar.
\end{aligned}
\tag{32}
$$

Fig. 14. Schematic of simple 1D argon plasma layout. A sin wave potential is applied to the left plate (100 V, f = 13.56 MHz) while the right plate is grounded. A sheath region is expected to exist near the electrodes where the net charge is non-zero.

The investigated problem is described in Fig. 14 with a small region of space $L = 2$ cm separating two infinitely large plates. One plate is grounded while another plate has an applied potential of 100 V oscillating according to a sinewave with frequency of 13.56 MHz. The gas separating the plates is of pressure $P = 10$ (Torr) with temperature $T = 300$ (K) with initial number densities (electrons and argon ions) of $n_e = n_p = 1E16$ m^{-3}. The applied potential varies according to a sin wave with frequency 13.56 MHz. Boundary conditions depend on the species: neutral species are treated using Neumann across each surface while charged species employ the following flux:

$$\Gamma_i = a \cdot \mu_i E n_i + \frac{1}{4} n_i v_{i,th},$$

$$\Gamma_e = a \cdot \mu_e E n_e + \frac{1}{4} n_e v_{e,th},$$

$$v_{i,e,th} = \sqrt{\frac{8 k_B T_e}{\pi m_{i,e}}},$$

(33)

where a in this case is an integer dependent on the direction of the flux under the influence of the electric field ($a = 1$ if μE points toward the boundary, $a = 0$ otherwise). The initial condition is advanced in an unsteady time-stepping procedure until the pseudo-steady state is reached. This result is shown in Fig. 15 compared to a conventional second order TVD scheme using the same solution parameters. The electrons, being very light and easily influenced by the electric field, tend to move back and forth across the region between the plates. This motion can be demonstrated by examining the distribution of electrons at various stages during the RF cycle.

Due to the very large electron convective velocities present (and resulting large Peclet numbers), the time step size must be restricted to quite a low number to ensure electrons do not transverse more than one cell in any given time step. In addition, in the sheath regions where large electric fields are present, the upwind feature of HLLG is prevalent: usually only ever the left or right flux is used directly since the convective speeds are so large. These two features of this flow reveal that the pseudo-steady state for both the HLLG and the conventional second order TVD scheme are almost indistinguishable. However, the unsteady progression to steady state is not: the HLLG scheme requires more RF cycles to reach the pseudo-steady state due to the reduced numerical dissipation in the scheme. In regions just outside the sheath region (where electric fields are very low), the solution is diffusion-bound. In this instance, the accuracy of HLLG provides an excellent solution; however, the increased number of RF cycles is required to reach the pseudo-steady state, despite the increase in accuracy. However, HLLG may become important in several transient simulations of discharge problems.

4. Conclusion

Presented is the derivation of the integral form of the HLL flux expressions which are then applied with spatially reconstructed values of conserved properties over cell widths. The obtained flux expressions, referred to as HLLG fluxes, proves that conventional extension to higher order through reconstruction at cell interfaces is mathematically inconsistent with the assumptions employed during the flux derivation and effectively results in an over-reconstruction of solution properties. The resulting flux expressions demonstrate that several reconstruction locations are required within the cell width as opposed to the single reconstruction location at the cell interface. Through solutions of the Euler and shallow water equations, conventional extension of HLL to second order using various limiting functions is demonstrated to produce oscillations while the mathematically complete extension employed by HLLG is shown to be less prone to such oscillations. The method is finally applied to the simulation of Argon RF plasma and compared to a conventional second order TVD method. In the course of the simulation, very large Peclet numbers are encountered in the sheath regions, causing the HLLG scheme effectively reduces to a conventional second order upwind scheme. Thus, the comparison between the HLLG and conventional scheme shows virtually identical results, demonstrating that the additional accuracy present in HLLG flux expressions may not be
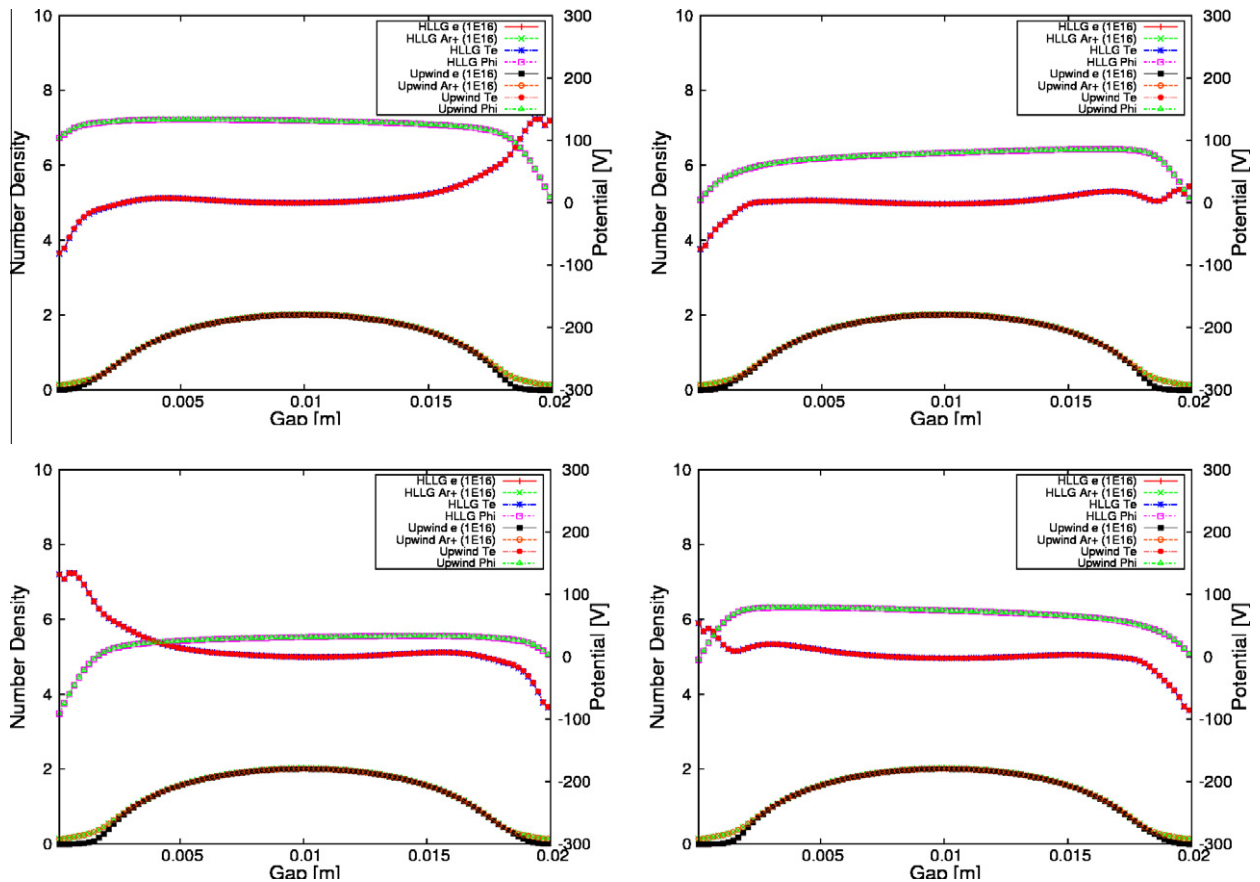
Fig. 15. Comparison of solutions from proposed HLLG scheme and a conventional second order TVD scheme applied to the solution of the fluid modeling equations. Results are shown for the pseudo-steady state at various points during the RF cycle – 0 (top, left), $\pi/2$ (top, right), π (bottom, left) and $3\pi/2$ (bottom, right). Results show number densities of Ar, Ar^+, Ar^m and e^- as a function of location between the plates, electron temperature and potential field. The gradient of the potential field (i.e. the electric field) is very low in regions outside the sheath regions.

essential for the pseudo-steady plasma simulations. However, this additional desired accuracy may be required for plasma simulations of differing configuration outside the scope of this investigation.

References

[1] S.K. Godunov, Finite difference method for the numerical computation of discontinuous solutions of the equations of fluid dynamics, Math. Sbornik 47 (1959) 271–306.
[2] A. Harten, P.D. Lax, B. van Leer, On upstream differencing and Godunov-type schemes for hyperbolic conservation laws, SIAM Rev. 25 (1) (1983) 35–61.
[3] E.F. Toro, Riemann Solvers and Numerical Methods for Fluid Dynamics, Springer-Verlag, New York, 1997.
[4] D.M. Causon, D.M. Ingram, C.G. Mingham, G. Yang, R.V. Pearson, Calculation of shallow water flows using a Cartesian cut cell approach, Adv. Water Res. 23 (5) (2000) 545–562.
[5] D.M. Ingram, D.M. Causon, C.G. Mingham, Developments in Cartesian cut cell methods, Math. Comput. Simul. 61 (3) (2003) 561–572.
[6] E.F. Toro, M. Spruce, W. Speares, Restoration of the contact surface in the HLL-Riemann solver, Shock Waves 4 (1) (1994) 25–34.
[7] P.L. Roe, Characteristic-based schemes for the Euler equations, Ann. Rev. Fluid Mech. 18 (1986) 337–365.
[8] B. van Leer, Towards the ultimate conservative difference scheme. III: Upstream-centered finite-difference schemes for ideal compressible flow, J. Comput. Phys. 23 (1977) 263–275.
[9] M.R. Smith, H.M. Cave, J.-S. Wu, M.C. Jermy, Y.-S. Chen, An improved quiet direct simulation method for Eulerian fluids using a second order scheme, J. Comput. Phys. 228 (6) (2009) 2213–2224.
[10] B. van Leer, Towards the ultimate conservative difference scheme, V. A second order sequel to Godunov's method, J. Comput. Phys. 32 (1979) 101–136.
[11] N.E. Kolgan, Application of the minimum-derivative principle in the construction of finite-difference schemes for numerical analysis of discontinuous solutions in gas dynamics, Uchenye Zapiski TsaGI [Sci. Notes of Central Inst. of Aerodynamics] 3 (6) (1979) 68–77 (in Russian).
[12] N.E. Kolgan, Finite-difference schemes for computation of three dimensional solutions of gas dynamics and calculation of a flow over a body under an angle of attack, Uchenye Zapiski TsaGI [Sci. Notes of Central Inst. of Aerodynamics] 6 (2) (1975) 1–6 (in Russian).

[13] V.A. Titarev, E.F. Toro, ADER schemes for three-dimensional non-linear hyperbolic systems, J. Comput. Phys. 204 (2) (2005) 715–736.
[14] M. Ben-Artzi, J.-Q. Li, G. Warnecke, A direct Eulerian GRP scheme for compressible fluid flows, J. Comput. Phys. 218 (1) (2006) 19–43.
[15] E. Han, J.-Q. Li, H.-Z. Tang, An adaptive GRP scheme for compressible fluid flows, J. Comput. Phys. 229 (5) (2010) 1448–1466.
[16] J.-Q. Li, G.-Z. Chen, The generalized Riemann problem method for the shallow water equations with bottom topography, Int. J. Numer. Methods Eng. 65 (6) (2005) 834–862.
[17] R.J. LeVeque, Finite Volume Methods for Hyperbolic Problems, Cambridge University Press, 2002.
[18] M.R. Smith, M.N. Macrossan, M.M. Abdel-Jawad, Effects of direction decoupling in flux calculation in finite volume solvers, J. Comput. Phys. 227 (8) (2008) 4142–4161.
[19] M. Cada, M. Torrilhon, Compact third-order limiter functions for finite volume methods, J. Comput. Phys. 228 (11) (2009) 4118–4145.
[20] C.-W. Shu, S. Osher, Efficient implementation and essentially non-oscillatory shock capturing schemes II, J. Comput. Phys. 126 (1989) 32–87.
[21] P. Woodward, P. Collela, The numerical simulation of two-dimensional fluid flow with strong shocks, J. Comput. Phys. 54 (1984) 115–174.
[22] SIGLO, BOLSIG: user-friendly Boltzmann solver from the SIGLO series, Webpage last visited on 5th Feb, 2010. Available from: <http://www.siglo-kinema.com/bolsig.htm>.
[23] H.C. Kim, F. Iza, S.S. Yang, M. Radmilović-Radjenović, J.K. Lee, Particle and fluid simulations of low-temperature plasma discharge: benchmarks and kinetic effects, J. Phys. D: Appl. Phys. 38 (2005) 283–301.
[24] D. Herrebout, A. Bogaerts, M. Yan, R. Gijbels, W. Goedheer, E. Dekempeneer, One-dimensional fluid model for an rf methane plasma of interest in deposition of diamond-like carbon layers, J. Appl. Phys. 90 (2) (2001) 570–579.
[25] R.B. Bird, W.E. Stewart, E.N. Lightfoot, Transport Phenomena, second ed., John Wiley & Sons, 2007.
[26] M. Hayashi, Bibliography of Electron and Photon Cross Sections with Atoms and Molecules Published in the 20th Century: Argon, Technical Report NIFS-DATA-72, National Institute for Fusion Science, Japan, 2003.
[27] E.A. Bogdanov, A.A. Kudryavtsev, L.D. Tsendin, R.R. Arslanbekov, V.I. Kolobov, V.V. Kudryavtsev, The influence of metastable atoms and the effect of the nonlocal character of the electron distribution on the characteristics of the positive column in an argon discharge, Tech. Phys. 49 (6) (2004) 698–706.
[28] T.V. Rakhimova, O.V. Braginsky, V.V. Ivanov, T.K. Kim, J.T. Kong, A.S. Kovalev, D.V. Lopaev, Y.A. Mankelevich, O.V. Proshina, A.N. Vasilieva, Experimental and theoretical study of RF plasma at low and high frequency, IEEE Trans. Plasma Sci. 34 (3) (2006) 867–877.
[29] M.W. Kiehlbauch, D.B. Graves, Modeling argon inductively coupled plasmas: the electron energy distribution function and metastable kinetics, J. Appl. Phys. 91 (6) (2002) 3539.